RSC Advances

PAPER

View Article Online
View Journal | View Issue

Cite this: *RSC Adv.*, 2021, **11**, 11900

Copper–CNT interfacing with Cu-doped polydopamine in CNT carpet: copper nucleation and resistance decrease upon soft annealing

Antoine Duhain, *[ab] Jérôme Guillot, [a] Guillaume Lamblin[a] and Damien Lenoble[a]

In recent years, Cu–CNT composites have attracted much attention due to their remarkable properties, in comparison to pure copper, such as higher ampacity and a lower thermal coefficient of resistance. However, the fabrication of an efficient Cu–CNT composite is still challenging, mainly due to the high cuprophobicity of CNTs. To strengthen the chemical interactions between Cu and CNTs, we propose using a Cu-doped polydopamine coating as an interface between CNTs and metallic copper. This work reports on the nucleation of copper particles on the surface of MWCNTs that are coated with Cu-doped polydopamine after annealing in an inert atmosphere at 573, 673 and 773 K. We show, for the first time to the best of our knowledge, that the polydopamine coating oxidizes during annealing and efficiently reduces Cu ions into metallic Cu. Interestingly, the sheet resistance of coated CNT carpets can be reduced by 33 and 37.6% after annealing at 573 and 773 K, respectively. Furthermore, the sheet resistance decrease does not depend on the size of copper particles (diameter ranging from 13 to 27 nm) or their surface density (from 2.27×10^{10} to 5.7×10^{8} particles per cm^2). This sheet resistance drop is mainly attributed to the appearance of pyridinic nitrogen in the Cu-doped polydopamine structure after annealing at 673 K and above. Finally, we measure a negative temperature coefficient of resistance for all of the CNT carpets.

Received 3rd November 2020
Accepted 22nd February 2021

DOI: 10.1039/d0ra09369f

rsc.li/rsc-advances

1 Introduction

In present times, the continuous miniaturization of electronic devices results in the problematic reduction of their lifetime. Indeed, the current density used in devices is close to the maximum current-carrying capacity (ampacity) of the metals used (copper, gold *etc.*).[1,2] Subramaniam *et al.* propose to tackle this issue by integrating copper–carbon nanotube (CNT) composites into their devices. They reported a strong increase in the ampacity (one hundred times) of such materials compared to pure copper.[3–5] Still, these results are controversial for such a material, acknowledging that the most recent literature discloses ampacity gains/losses ranging from 30% loss to 36% gain.[6–8] Such a large range of results demands further investigation related to the mechanisms governing the conductivity and ampacity of these materials. Among the critical parameters governing the conductivity and the ampacity of such composites, the electronic interactions of copper and CNT orbitals are instrumental. Therefore, new avenues are needed to eliminate the strong cuprophobicity of CNTs.[9–11] Among recent strategies, Guo *et al.* presented an interesting strategy using Cu nanoparticles, grown by electroless plating on a CNT surface, to enhance the interfacial bonding between CNTs and Al by reducing the misfit strain between the Al matrix and CNTs.[12] Daneshvar *et al.* showed that copper particles at the surface of functionalized CNTs can enhance the conductivity of CNT carpets. In particular, they demonstrated a higher affinity between copper and CNTs when a thiol-based functional group was used. However, electroless plating was used to grow Cu particles on the CNT surface and the use of palladium seeding was required.[13] In spite of promising results demonstrating the efficiency of polydopamine (Pda) to coat CNT,[14] we propose, for the first time to the best of our knowledge, the use of Pda doped by Cu to efficiently nucleate and interface metallic copper materials with CNTs. Pda was increasingly studied in 2007 after Lee *et al.* reported that Pda could be used as a seed layer for silver electroless deposition, leading to the spontaneous reduction of Ag(I) into Ag(0).[15,16] Pda coating is an excellent candidate for CNT dispersion in aqueous solution due to the excellent adhesion and hydrophilic properties of Pda.[14,17] Furthermore, metal ions can be strongly coordinated by the functional groups of Pda[16,18] and Li *et al.* reported the possibility of nucleating copper particles from Cu-doped Pda when annealed.[19] This work provides a thorough analysis of the nucleation and growth of copper particles on CNTs coated with copper-doped polydopamine, revealing the conductivity and

[a]*Materials Research and Technology Department, Luxembourg Institute of Science and Technology, Rue du Brill 41, L-4422, Belvaux, Luxembourg. E-mail: antoine.duhain@list.lu; Tel: +352-275888-4551*

[b]*University of Luxembourg, Limpertsberg Campus, 162a avenue de la Faïencerie, L-1511, Luxembourg*

temperature coefficient of resistance (TCR), which are suitable for the further fabrication of Cu–CNT composites. We first characterize the chemistry and morphology of copper grown on CNTs in order to further investigate the mechanisms related to such growth. Afterwards, we cross-link these results with variations of sheet resistance and TCR induced by the thermal annealing of the CNT carpets.

2 Materials and methods

2.1 CNT preparation

Commercial multi-walled carbon nanotubes (MWCNTs) (average diameter 80–90 nm; average length 200 μm) were bought from NanoTechLabs, Inc. (NTL). Dopamine hydrochloride and nitric acid (65%) were bought from Sigma-Aldrich. Hydrochloric acid (37%, AnalaR NORMAPUR) and ethanol absolute (>99.8% AnalaR NORMAPUR) were bought from VWR.

2.1.1 CNT oxidization. Following a protocol inspired by Rosca *et al.*,[20] 350 mg of CNTs were oxidized through sonication in 50 ml of nitric acid 52% for 30 minutes at room temperature. Oxidized CNTs were then filtrated and rinsed with DI water. Oxidation in nitric acid produces principally carboxylic groups at the CNT surface.[20]

2.1.2 Pda coating on CNTs (CNT@Pda). A protocol inspired by Shi *et al.*[14] was used to prepare Pda-coated CNT samples. 150 mg of oxidized CNTs were dispersed in 937.5 ml of a solution of dopamine hydrochloride (DA) (0.1 mg ml^{-1}). The solution was ultra-sonicated for 10 s then vigorously stirred for 25 min in the solution in order to promote the adsorption of the DA monomers on the CNT surface, which occurred due to van der Waals and π–π stacking interactions between the aromatic dopamine and the sp^2 hybridized carbon of the CNTs.[14] Furthermore, CNT oxidation can promote the adsorption of DA monomers on the CNTs due to the formation of hydrogen bonds between carboxylic groups at the CNT surface and the catechol groups of dopamine.[21] DA polymerization was triggered by the addition of 562.5 ml Tris–HCl (0.01 M) and the solution was successively ultra-sonicated for 10 s. It was then vigorously stirred for 24 h. 18.75 ml of NaOH (1 M) was added to the dispersion and the CNTs were recovered by filtration. The CNTs were then dispersed in 100 ml of absolute ethanol (EtOH). The CNT dispersion was then filtered, rinsed twice with 200 ml EtOH and re-dispersed in 100 ml EtOH.

2.1.3 Cu-doped Pda coating on CNTs (CNT@PdaCu). To prepare CNT@PdaCu, 150 mg of oxidized CNTs were coated using the same protocol as shown above, except that $CuSO_4 \cdot 5H_2O$ was added to the dopamine solution (2.4 mM and 0.5 mM, respectively). Cu(II) was expected to be chelated by the amine and catechol groups of DA.[16,18] In addition to the hydrogen bonding between DA and the oxidized CNT surface, the –COOH groups were also expected to provide a binding site for Cu(II) ions and promote the adsorption of the DA–Cu(II) complexes.[13,16,18]

2.1.4 Annealing of samples. The CNT annealing experiments were performed in a Carbolite Gero CWF furnace upgraded with an internal retort, allowing the atmosphere to be controlled. CNT@PdaCu samples were annealed in a fully inert atmosphere (Ar), rising from room temperature to 573, 673 and 773 K at a 5 K min^{-1} heating rate. When the desired temperature was reached, the furnace was cooled down overnight to room temperature.

2.2 Physical characterisation

2.2.1 X-ray photoelectron spectroscopy (XPS). The Cu 2p, N 1s, C 1s and O 1s photoelectron spectra and Cu LMM Auger electron spectra of samples given in Table 1 were acquired using Kratos Axis Ultra DLD apparatus equipped with a monochromatic Al Kα X-ray source running at 150 W (10 mA, 15 kV). The spectroscopy was carried out on an analysis area set to 300 × 700 μm^2 with 20 eV pass energy for the narrow scans, leading to a FWHM of 0.6 eV on the Ag $3d_{5/2}$ line of a cleaned reference silver foil. The electron spectrometer had previously been calibrated on the Cu $2p_{3/2}$ and Au $4f_{5/2}$ lines at 932.6 eV and 84.0 eV respectively. Without any further charge correction, the main C 1s component, corresponding to the sp^2 carbon atoms in the CNTs, is found at 284.35 ± 0.05 eV for every sample. The spectra were analysed with CasaXPS software. It has been verified that annealing the oxidized CNTs at 773 K leaves the C 1s line shape unchanged. This spectrum has subsequently been used as the CNT component in the C 1s peak reconstruction of all samples (Fig. 3). It allowed us to discriminate the oxidized CNT contribution from the polydopamine coating contribution. The relative intensities of the C–N and C=N components in C 1s were fixed using their atomic percentage ratio, which was determined from the N 1s spectra and the nitrogen percentage in the sample. Except for the oxidized CNT, the O 1s spectra present a large tail at the high binding energies, over 535.0 eV, a feature of the sodium Auger peaks.[22] The sodium contribution has been fitted with a single component centred at 534.8 ± 0.1 eV. The intensity of this peak represents between 12 and 20 percent of all of the O 1s peaks and its evolution is in accordance with the sodium amount detected in the samples after the various synthesis steps and thermal treatments. This contribution has systematically been removed from the O 1s peaks to accurately determine the elemental composition. The low % of Cl detected in the CNT@PdaCu samples (Table 2) results from contamination by the buffer (Tris–HCl) and/or residual hydrochloride salts coming from the dopamine hydrochloride. Although there were two rinsing steps with EtOH after the polymerization step of DA, small quantities of some salts can sometimes remain in the CNT@PdaCu filtered layer. The detection of Cl in the

Table 1 Summary of the characterized samples

	XPS	SEM/STEM	HIM-SIMS	DSC	TCR/R_s
Oxidized CNTs	✗				✗
Oxidized CNTs 773 K	✗				✗
CNT@Pda	✗			✗	✗
CNT@Pda 773 K					✗
CNT@PdaCu	✗	✗		✗	✗
CNT@PdaCu 573 K		✗			✗
CNT@PdaCu 673 K	✗	✗			✗
CNT@PdaCu 773 K	✗	✗	✗		✗

Table 2 XPS elemental composition in atomic percentage

	C (%)	Cl (%)	Cu (%)	N (%)	Na (%)	O (%)
Oxidized CNTs	97.5	0.0	0.1	0.3	0.0	2.1
CNT@Pda	76.4	0.2	0.0	5.1	4.2	14.1
CNT@PdaCu	69.0	0.2	2.2	5.8	3.8	19.0
CNT@PdaCu 673 K	77.5	1.3	2.0	7.2	2.1	9.9
CNT@PdaCu 773 K	81.3	1.1	1.5	6.5	2.0	7.6

annealed samples is therefore not specifically linked to the annealing process.

2.2.2 Scanning electron microscopy (SEM) and scanning transmission electron microscopy (STEM). SEM and STEM (FEI; Helios NanoLab™ 650) were used to record high resolution images of the CNTs. CNTs were deposited on typical holey carbon-supported Cu grids. Pictures were taken using a 1.0 μm field of view with an acceleration voltage of 30 kV. Pictures were post-processed with ImageJ to estimate the number of particles per square centimetre and the nuclei size distribution. The mean nuclei density and error bars shown in Fig. 6a are calculated from all of the distinct images analysed for each sample. Catalyst particles typically used to grow the CNTs are present in all samples; for this reason, the mean size and density of copper nuclei were extracted by subtracting the catalyst background calculated from CNT@PdaCu before annealing.

2.2.3 Helium ion microscopy-secondary ion mass spectroscopy (HIM-SIMS). HIM-SIMS analysis was performed with a Helium Ion Microscope instrument (Zeiss, Peabody, MA, USA) coupled with a mass spectrometer developed at the Luxembourg Institute of Science and Technology.[23] Electron microscopy images were recorded using a 25 kV helium beam and a primary current of 0.5 pA. The analytical information was provided by the secondary ion mass spectroscopy (SIMS) technique. SIMS measurements were acquired in imaging mode using a primary bombardment of Ne^+ accelerated at 20 kV. The probe ranged from 20 to 40 nm in diameter, with an intensity of 3 pA. The raster size was $5 \times 5\ \mu m^2$ for a matrix of 512×512 pixels.[2] This technique was specifically used to investigate the spatial distribution of chemical elements at the surface of CNT@PdaCu annealed at 773 K compared to reference oxidized CNTs.

2.2.4 Differential scanning calorimetry (DSC). DSC (Mettler Toledo DSC3+) was used to measure the variation of enthalpy during CNT annealing and was carried out in Ar gas to reproduce the annealing conditions. 11.5 mg of CNT@Pda and 5 mg of CNT@PdaCu were placed in an aluminium crucible. Due to the small quantity of reacting material, the samples were heated with a 20 K min^{-1} ramp to 673 K (instead of the 5 K min^{-1} used during the annealing) in order to increase the DSC signal intensity.[24]

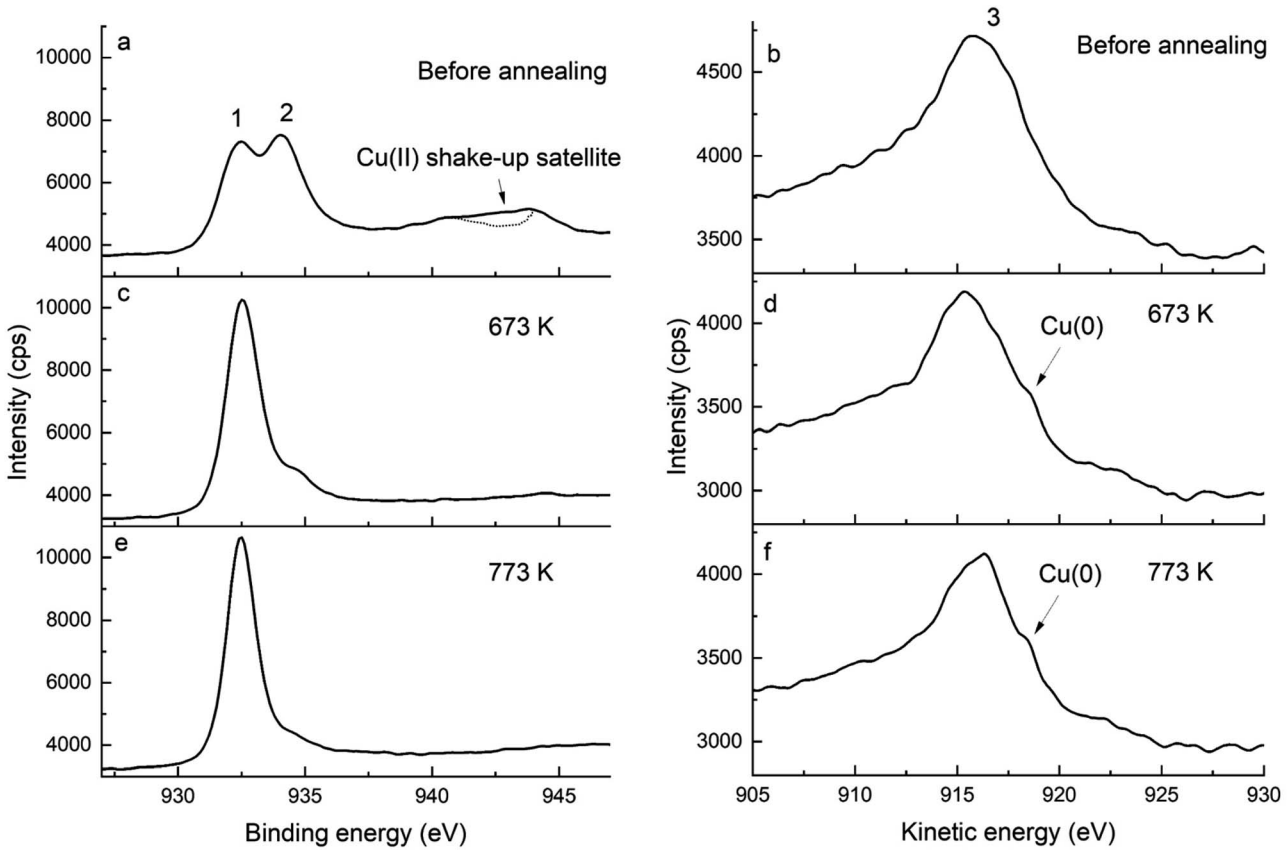

Fig. 1 Cu 2p (left) and Cu LMM (right) spectra of (a and b) CNT@PdaCu, (c and d) CNT@PdaCu annealed at 673 K and (e and f) CNT@PdaCu annealed at 773 K. (1) peak at 932.45 eV related to Cu(I) species, (2) peak at 934.0 eV related to Cu(II) species, and (3) peak at 915.8 eV related to Cu(I) and Cu(II) species.

2.2.5 Temperature coefficient of resistance (TCR) and sheet resistance measurements. TCR measurements were carried out between 298 and 433 K with a four-probe setup coupled with a temperature-controlled hot plate. The probes have a space of 1 mm and measurements were performed on 1 × 1 cm CNT carpet samples. Those samples were obtained through the filtration of the CNT solutions (oxidized, CNT@Pda

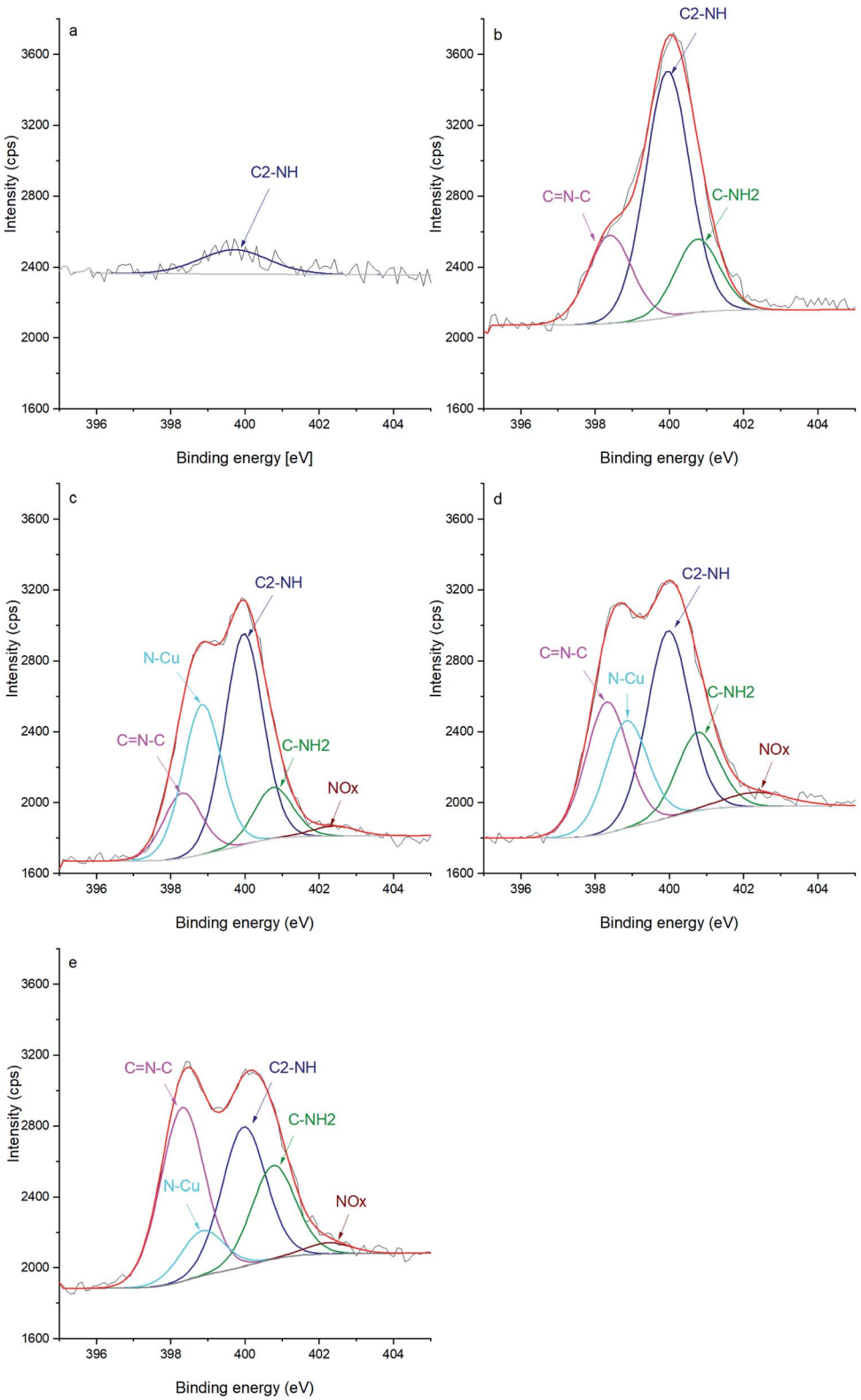

Fig. 2 N 1s spectra of (a) oxidized CNT, (b) CNT@Pda, (c) CNT@PdaCu, (d) CNT@PdaCu annealed at 673 K and (e) CNT@PdaCu annealed at 773 K.

and CNT@PdaCu) followed by the peeling of the CNT layer from the filtration membrane.

The sheet resistance of the CNT carpets was measured at room temperature. As the thickness of CNT carpets is difficult to measure accurately, the one-to-one comparison of sheet resistance between samples is not reliable. Thus, we decided to compare the drop in resistance of the CNT carpets after annealing at 573, 673 and 773 K to their resistance before annealing. The drop in resistance is expressed as $100 \times (1 - R_{\text{annealed}}/R_{\text{notannealed}})$ %.

3 Results and discussion

XPS is a powerful means to determine the oxidation state of metals and their oxides, hence it was used to investigate the mechanisms of the growth of copper particles upon the annealing of Cu-doped Pda coated CNTs. Fig. 1 displays the Cu 2p and Cu LMM spectra of Cu-doped Pda before and after annealing at 673 and 773 K. The presence of copper in the Pda coating of CNT@PdaCu is confirmed by XPS (Fig. 1a and b). The shake-up satellite (Fig. 1a) is a clear indication of the presence of Cu(II).[25] Peak 1, at 932.45 eV, is attributed to Cu(I). The possibility of Cu(I) being present as CuCl was excluded using the elemental composition (Table 2), which showed that CuCl cannot present a major contribution to the Cu 2p line. One can notice that the peak position has slightly shifted compared to the Cu_2O bulk value (932.18 eV (ref. 25)). This energy shift may be attributed to the Cu(I) ions coordinated to the catechol/quinone/amine groups of Pda.[16,18] Similarly, we attribute the peak at 934 eV to Cu(II) being coordinated by Pda. Indeed, the lack of indentation in the shake-up satellite (see the dotted line in Fig. 1a) precludes the presence of CuO.[25] We might conclude that Cu(II) and Cu(I) are coordinated in the polydopamine coating and that the Cu(II) introduced from $CuSO_4$ is partially reduced into Cu(I) during the dopamine polymerization. This reduction is attributed to the several oxidation steps involved in the dopamine polymerization. In particular, the oxidation of catechol to quinone releases two electrons which can reduce the chelated metal ions.[16,26]

Additionally, the chemical evolution of the samples can be demonstrated by the N 1s, C 1s and O 1s spectra (Fig. 2, 3 and 4 respectively). The reference sample (Fig. 2a) features CNTs doped with nitrogen due to oxidation in nitric acid (peak at 400 ± 0.1 eV associated with C2–NH).[27–30] One can recall that in the CNT@Pda sample (Fig. 2b), the C2–NH (pyrrolic nitrogen) and C=N–C (pyridinic nitrogen) components feature cyclic units of

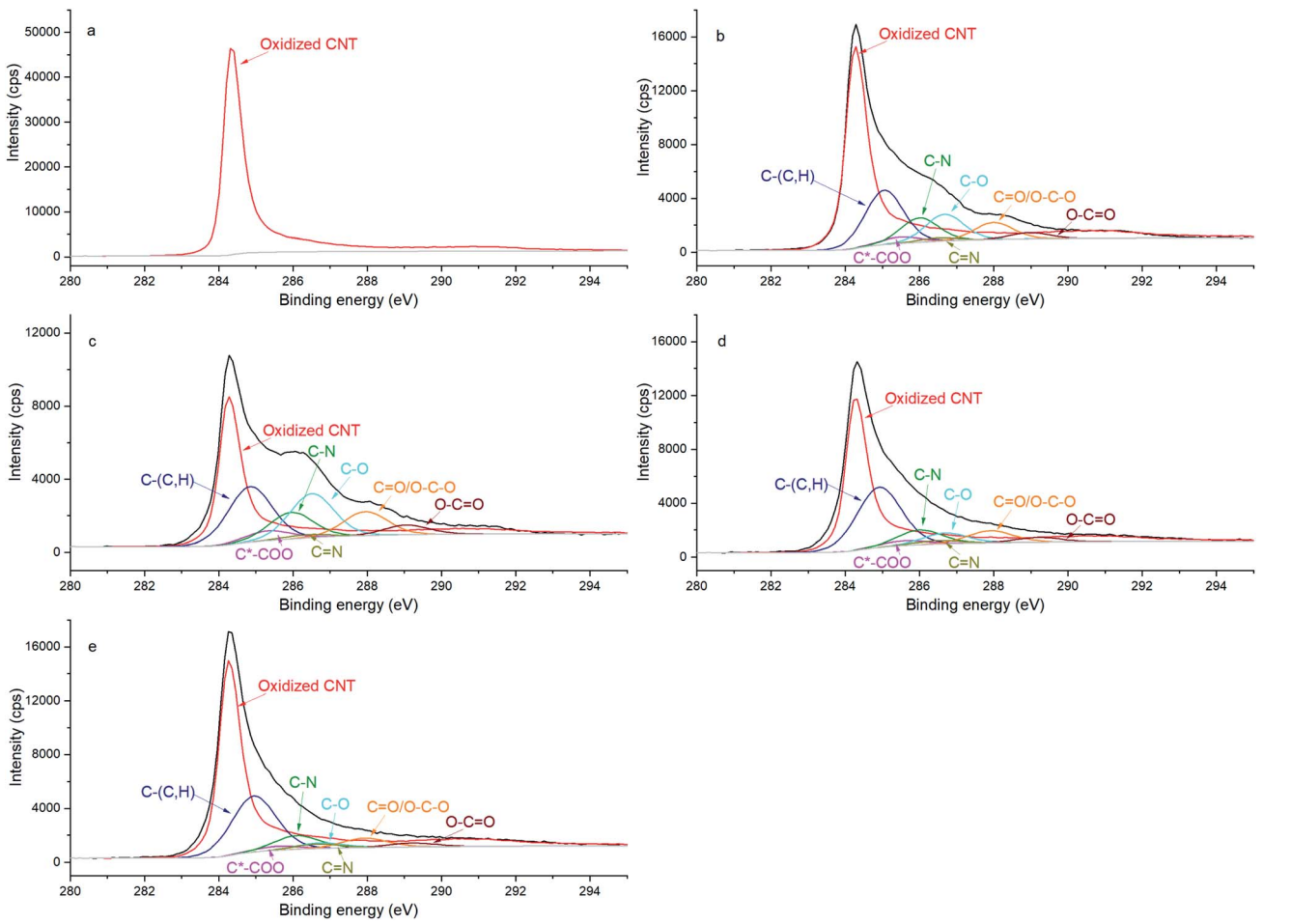

Fig. 3 C 1s spectra of (a) oxidized CNT, (b) CNT@Pda, (c) CNT@PdaCu, (d) CNT@PdaCu annealed at 673 K and (e) CNT@PdaCu annealed at 773 K.

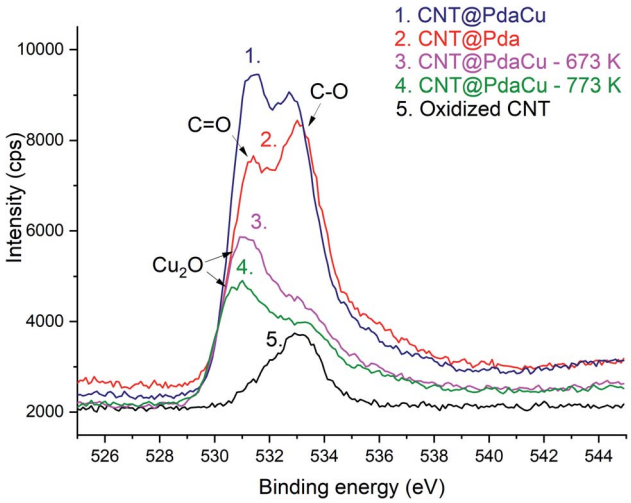

Fig. 4 O 1s spectra of (1) CNT@PdaCu, (2) CNT@Pda, (3 and 4) CNT@PdaCu annealed at 673 and 773 K, respectively, and (5) oxidized CNTs.

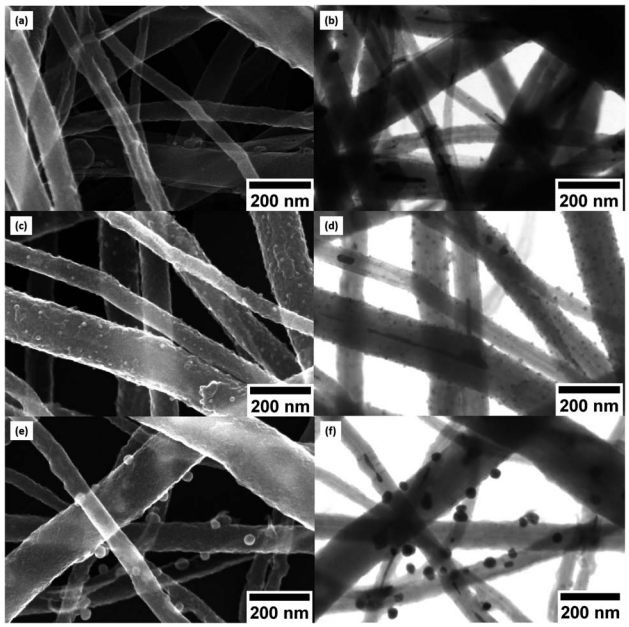

Fig. 5 (a) SEM and (b) STEM image of CNT@PdaCu. (c) SEM and (d) STEM image of CNT@PdaCu annealed at 573 K. (e) SEM and (f) STEM image of CNT@PdaCu annealed at 773 K.

Pda formed *via* the Michael addition reaction.[16] The CNT@PdaCu sample (Fig. 2c) features a peak at 398.8 eV attributed to nitrogen–copper interactions.[27,29,31] Interestingly, the relative contribution of the Cu–N component (Table 3) decreases upon annealing from 30.5% (CNT@PdaCu) to 20.2% (CNT@PdaCu annealed at 673 K) and towards 8.8% (CNT@PdaCu annealed at 773 K) meaning that the amount of Cu ions chelated in Pda decreases as the annealing temperature increases. In the Cu 2p spectra (Fig. 1c and e), the thermal annealing of CNT@PdaCu at 673 and 773 K shows a drastic decrease of the shake-up satellite and peak at 934 eV, highlighting that Cu(II) is disappearing. The Cu LMM spectra (Fig. 1d and f) feature a shoulder at 918.5 eV, corresponding to the formation of Cu(0) during annealing.[25] We also observe a shift of peak number 3 from 915.8 to 916.4 eV at 773 K. We attribute this shift to the progressive surface oxidation of the grown copper particles (Fig. 5) into Cu_2O (which has an expected peak position of 917.0 eV).[32,33] As seen above in the N 1s spectra, the Cu–N chelation component still represents 8.8% of the nitrogen amount after annealing at 773 K. We might thus conclude that, after annealing at 773 K, Cu(I) is still partially coordinated in Pda while some Cu(I), in the Cu_2O form, appears at the copper nuclei surface due to exposure to air. The presence of C=N–C, N–Cu, C2–NH and C–NH2 components in Fig. 2d and e confirms the preservation of the Pda coating after annealing at 673 and 773 K. Nevertheless, the Pda structure is altered by the annealing; the C=N–C bonding (Table 3) in annealed CNT@PdaCu (25.4 and 38.4% at 673 and 773 K, respectively) is significantly higher than in non-annealed CNT@PdaCu (13.7%). The C2–NH contribution in CNT@PdaCu (43.3%) decreases when annealed at 673 and 773 K (35.9 and 30.6%, respectively). These results suggest a progressive suppression of pyrrolic nitrogen in favour of pyridinic nitrogen during annealing.[42,43]

The lower ratio (Table 4) of C–O/C=O in CNT@Pda (Fig. 3b) than in CNT@PdaCu (Fig. 3c) suggests that catechol/semiquinone groups are present in higher quantities than quinone when copper is coordinated in Pda. Barrett *et al.*[34] suggested that catechol groups could be partially protected by the coordination of metal ions during polymerization in alkaline conditions. Interestingly, when CNT@PdaCu samples are annealed at 673 and 773 K, the same ratio drops to 0.9 and 0.6, respectively, illustrating an even more important quinone component. We believe that the thermal treatment induces further oxidation of polydopamine, providing a continuous source of electrons that enable the efficient reduction of copper

Table 3 N 1s peak components and their relative contribution to the peak fit (%)

	C=N–C (%)	N–Cu (%)	C2–NH (%)	C–NH2 (%)	NOx (%)
Oxidized CNTs	0.0	0.0	100.0	0.0	0.0
CNT@Pda	21.9	0.0	60.9	17.2	0.0
CNT@PdaCu	13.7	30.5	43.3	10.1	2.4
CNT@PdaCu 673 K	25.4	20.2	35.9	14.5	4.1
CNT@PdaCu 773 K	38.4	8.8	30.6	19.6	2.7

Table 4 C 1s peak components, their relative contribution to the peak fit (%) and the ratio $\frac{C-O}{CaO}$

	CNT	C–(C, H)	C*–COO	C–N	C=N	C–O	C=O O–C–O	O–C=O	$\frac{C-O}{CaO}$
CNT@Pda	57.2%	16.9%	1.9%	7.5%	1.0%	8.2%	5.3%	1.9%	1.5
CNT@PdaCu	40.2%	19.2%	3.4%	9.2%	1.1%	15.2%	8.3%	3.4%	1.8
CNT@PdaCu 673 K	52.3%	26.1%	2.0%	6.3%	1.4%	4.6%	5.2%	2.0%	0.9
CNT@PdaCu 773 K	61.8%	22.4%	1.5%	5.4%	1.7%	2.1%	3.6%	1.5%	0.6

ions as revealed by the detailed analysis of the XPS spectra of copper. This conclusion is further supported by carefully analysing the O 1s spectra which evidences a drastic decrease of the C–O component of CNT@PdaCu (curve 1 in Fig. 4) after thermal treatment (curves 3–4 in Fig. 4). Finally, we could attribute the drop in oxygen (Table 2) from 19% before annealing to 7.6% after annealing at 773 K, respectively, to the catechol dehydration as suggested by Kong *et al.*[43]

One can note an evolution of the O 1s peak shape for Pda-coated CNTs (curves 2 and 5 in Fig. 4) which features an increase in both the O=C and O–C contributions, at 531.4 and 533 eV respectively,[35,36] corresponding to the catechol and quinone groups of the Pda. The Cu doping of the Pda coating (curve 1 in Fig. 4) leads to a higher component located at 531.4 eV and is attributed to Cu(II) chelated by Pda, as previously observed in the Cu 2p spectra. One can note a shift of this peak's maximum towards 531.1 and 531.0 eV when samples are annealed at 673 and 773 K, respectively. This shift is attributed to the appearance of Cu_2O at the surface of the Cu nanoparticles, as already seen in the Cu 2p spectra.[25,32,33,37,38]

Fig. 5a of CNT@PdaCu without annealing shows the distribution of CNTs with a diameter ranging from 33 to 195 nm. The same sample observed by STEM (Fig. 5b) shows inner particles (black spots) corresponding to the typical catalysts used to grow CNTs. We calculate the average diameter of catalyst to be around 18 nm, with a density of 6.8×10^9 particles per cm^2 (Fig. 6a and b). Catalysts are present in all analysed samples. Fig. 5c (CNT@PdaCu annealed at 573 K) reveals the growth of nuclei rather than a homogeneous coating distributed over the CNT surface. The STEM image (Fig. 5d) shows a strong contrast with the CNTs corresponding to those particles and enables their main features to be counted precisely: size and density. CNT@PdaCu annealed at 773 K (Fig. 5e) shows bigger particles on most of the CNTs except the largest one. Nevertheless, observations of other areas of the same sample have shown that the growth of particles is not dependent on the diameter of the CNT. The STEM image of the same sample in Fig. 5f further confirms the rather high material density (contrast-dependent) of the grown particles. Furthermore, additional image contrast enhancement reveals the growth of particles on the back side of the largest CNT. Only the images of the samples annealed at 573 and 773 K are presented here but similar observations can be made for the sample annealed at 673 K. After annealing at 573 K, one can observe a high particle density (2.27×10^{10} particles per cm^2) related to the appearance of a new population of nuclei with an average diameter of 13 nm (Fig. 6). When the sample is annealed at 673 K, the particle density remains almost the same (2.34×10^{10} particles per cm^2) while the mean diameter of the nuclei grows slightly (15 nm). At 773 K, the quantity of particles decreases drastically (5.7×10^8 particles per cm^2) while their average diameter shifts towards 27 nm. The small decrease of the Cu content detected by XPS during annealing (Table 2) is thus attributed to the gradual formation of copper nuclei with a diameter larger than the XPS probing depth (<10 nm).

Fig. 7 shows the comparative DSC measurements of the CNT@Pda and CNT@PdaCu samples in order to further understand the chemical mechanisms governing the nucleation of particles on the CNT surfaces. In both cases, the first

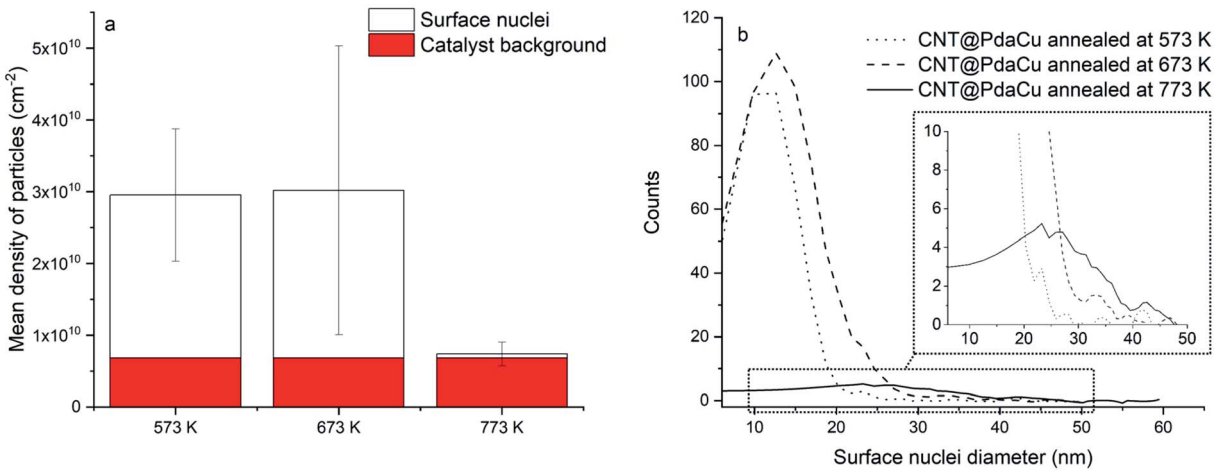

Fig. 6 (a) Mean density of particles and (b) nuclei size distribution.

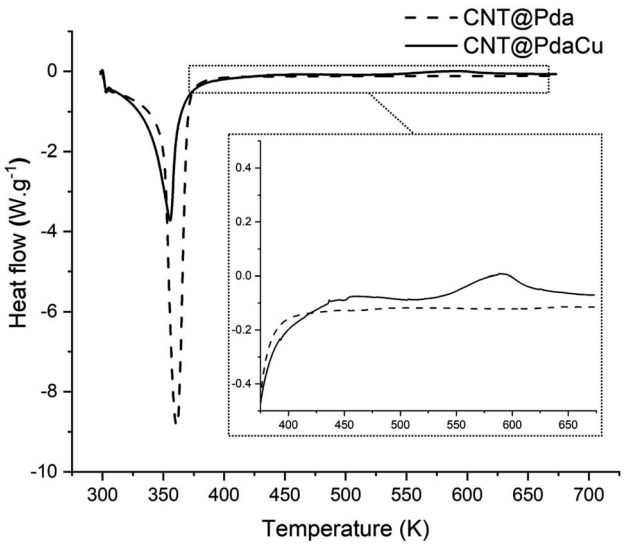

Fig. 7 Differential scanning calorimetry measurements of CNT@Pda and CNT@PdaCu. Inset: magnification showing the exothermic peak for the CNT@PdaCu sample.

endothermic peak below 373 K is attributed to the evaporation of ethanol contained in the Pda hydrophilic layer. The most specific feature of the CNT@PdaCu sample is the exothermic peak around 573 K. Li *et al.* have attributed this peak to the appearance of metallic nuclei during the annealing of Cu-doped Pda coated on fused silica.[39] In our case, this exothermic peak occurs between 540 K and 660 K and concurs with the observation of surface particles in the samples annealed at 573, 673 and 773 K. As shown by the Cu LMM spectra, the presence of metallic Cu is detected for samples annealed beyond 673 K. We believe that this peak might be related to the energy variation arising from the redox reaction between copper and Pda, as well as the decrease of free energy due to the reduction of the surface area of the Cu particles.[40] Fig. 8 a and b (electron microscopy and HIM-SIMS, respectively) highlight the presence of copper (in blue) and its homogeneous distribution on the CNT@PdaCu surface after annealing at 773 K.

Fig. 9a and b show a photograph and a SEM image, respectively, of a CNT@PdaCu carpet sample annealed at 673 K and used for the resistance measurements. The CNTs are

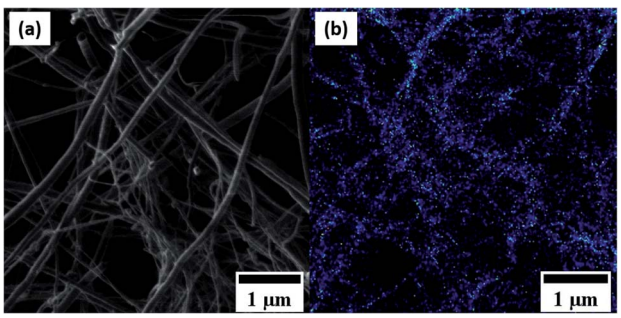

Fig. 8 (a) Secondary electron and (b) HIM-SIMS images of the same zone of CNT@PdaCu annealed at 773 K.

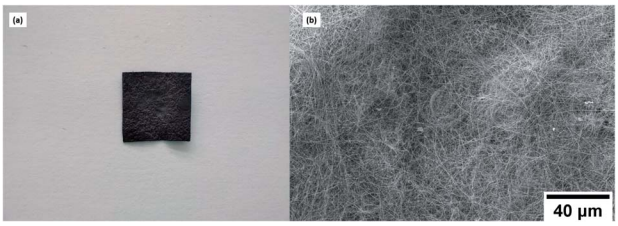

Fig. 9 (a) Photograph and (b) SEM image of the CNT@PdaCu carpet sample annealed at 673 K.

randomly oriented within a horizontal plane. All CNT carpet samples displayed a similar morphology. Table 5 summarizes the drop in resistance (at room temperature) of the CNT carpets after annealing at 573, 673 and 773 K, in comparison to their resistance before annealing. It shows that there is no drop in resistance for the oxidized CNT reference sample ($-8.8 \pm 12.0\%$). Lekawa-Raus *et al.* reported that a small increase of resistance could be observed in CNT fibers after annealing due to humidity removal.[41] One can observe a drop in resistance of $32.4 \pm 3.6\%$ for the CNT@Pda sample after annealing at 773 K. Several authors reported an increase in the conductivity of Pda after annealing,[42–44] which could explain the drop in resistance of the Pda-coated CNT carpet. There is no significant difference among the CNT@PdaCu samples annealed at 573, 673, and 773 K; indeed the resistance drops are 33 ± 1.3, 36.9 ± 6.7 and $37.6 \pm 12.2\%$, respectively. This means that the carpet resistance is independent of the copper particle size and density. One can recall that copper particles on the CNT surface have a high density with a smaller size at 573 K and are bigger with a lower density at 773 K (Table 6). Finally, there is no significant difference between CNT@Pda and CNT@PdaCu when both are annealed at 773 K. This is surprising since Li *et al.*[19] attributed the higher conductivity of a Cu-doped Pda coating (on fused silica) annealed at 873 K (in comparison to undoped Pda annealed at the same temperature) to the nucleation of copper particles in the Cu-doped Pda coating. In our case, the Cu 2p spectra showed that the copper particles are partially oxidized in Cu_2O after annealing at 773 K, which might explain the independence of the resistance from the particle size and density. The resistance decrease in the CNT@PdaCu samples is attributed to the progressive suppression of pyrrolic nitrogen (C2–NH) in favour of pyridinic nitrogen (C=N–C), as previously observed in Table 3.[42–44] As seen in Table 6, the temperature coefficient of

Table 5 Drop in resistance of the CNT carpet samples after annealing at 573, 673 and 773 K, in comparison to their resistance before annealing. The resistance drop is expressed as $100 \times (1 - R_{annealed}/R_{notannealed})$ %

Annealing temperature	Oxidized CNTs	CNT@Pda	CNT@PdaCu
573 K	—	—	$33 \pm 1.3\%$
673 K	—	—	$36.9 \pm 6.7\%$
773 K	$-8.8 \pm 12.0\%$	$32.4 \pm 3.6\%$	$37.6 \pm 12.2\%$

Table 6 Temperature coefficient of resistance of the CNT carpets before and after annealing at 573, 673 and 773 K

Annealing temperature	Oxidized CNTs	CNT@Pda	CNT@PdaCu
Not annealed	$-1.44 \times 10^{-3} \pm 3.17 \times 10^{-5}$	$-2.73 \times 10^{-3} \pm 1.89 \times 10^{-4}$	$-2.21 \times 10^{-3} \pm 4.59 \times 10^{-4}$
573 K	—	—	$-1.85 \times 10^{-3} \pm 9.09 \times 10^{-5}$
673 K	—	—	$-1.73 \times 10^{-3} \pm 1.03 \times 10^{-4}$
773 K	$-1.44 \times 10^{-3} \pm 4.05 \times 10^{-5}$	$-2.26 \times 10^{-3} \pm 1.39 \times 10^{-4}$	$-2.35 \times 10^{-3} \pm 1.02 \times 10^{-4}$

resistance is negative for the annealed and non-annealed oxidized CNT reference samples. Interesting work from Naeemi *et al.*[45,46] theoretically attributed the negative TCR of MWCNTs to their large diameter. The TCR of the CNT@Pda sample slightly increased when annealed at 773 K, while the TCR of the CNT@PdaCu samples remained apparently unaffected after annealing at 573, 673 and 773 K. The conductivity of polydopamine displayed a $\log(\sigma) \propto -1/T$ semi-conductor behaviour in a dry environment[47,48] and could partially contribute to the negative TCR of the coated CNTs.

4 Conclusions

We demonstrated the nucleation and growth of metallic copper nanoparticles onto the surface of CNTs coated with Cu-doped polydopamine when annealed in an Ar environment at temperatures varying from 573 to 773 K. Based on the XPS characterisation of these materials, the copper nucleation mechanism is attributed to the reduction of Cu ions by the electrons released during the oxidation of catechol into quinone moieties upon annealing. The nuclei are quite homogeneously distributed on the CNT surface, independent of the CNT diameter. The nuclei diameters range from 13 to 27 nm after annealing at 573 and 773 K, respectively, and the particle density drops from 2.27×10^{10} to 5.7×10^{8} particles per cm^2, respectively. The carpets of CNTs coated with Cu-doped Pda displayed a decrease in resistance quite independent of the annealing temperature (ranging from 33 ± 1.3 to $37.6 \pm 12.2\%$). This resistance drop upon annealing is attributed to pyridinic nitrogen formation in the Pda structure. Furthermore, this variation of resistance is independent of the growth of the copper particles. We believe that it could be attributed to the progressive oxidation of copper particles when exposed to air. In addition, we showed a negative TCR for our metallic CNT carpet, which is promising for obtaining low TCR Cu–CNT composites. The easy nucleation of metallic copper particles at the surface of the CNTs, combined with the negative TCR and drop in resistance after soft annealing, are particularly promising material features to fabricate high performance Cu–CNT composite materials.

Conflicts of interest

There are no conflicts of interest to declare.

Acknowledgements

This work was financially supported by the Luxembourg National Research Fund (C-PPP16/MS/11515319), the Luxembourg Institute of Science and Technology, and Circuit Foil Luxembourg Sàrl. We thank J. N. Audinot for HIM-SIMS data acquisition, R. Vaudemont and B. Marcolini for DSC data acquisition, and L. Auguin and E. Collard for proofreading the text.

References

1 J. Lienig and M. Thiele, *Fundamentals of Electromigration-Aware Integrated Circuit Design*, Springer Publishing Company, 1st edn, 2018.
2 K. Tu and A. M. Gusak, *J. Appl. Phys.*, 2019, **126**, 075109.
3 C. Subramaniam, T. Yamada, K. Kobashi, A. Sekiguchi, D. N. Futaba, M. Yumura, *et al.*, *Nat. Commun.*, 2013, **4**, 2202.
4 C. Subramaniam, Y. Yasuda, S. Takeya, S. Ata, A. Nishizawa, D. N. Futaba, *et al.*, *Nanoscale*, 2014, **6**, 2669–2674.
5 C. Subramaniam, A. Sekiguchi, T. Yamada, D. N. Futaba and K. Hata, *Nanoscale*, 2016, **8**, 3888–3894.
6 R. Sundaram, T. Yamada, K. Hata and A. Sekiguchi, *Sci. Rep.*, 2017, **7**, 9267.
7 J. Shuai, L. Xiong, L. Zhu and W. Li, *Composites, Part A*, 2016, **88**, 148–155.
8 G. Mokry, J. Pozuelo, J. J. Vilatela, J. Sanz and J. Baselga, *Nanomaterials*, 2019, **9**, 383.
9 D. Janas and B. Liszkab, *Mater. Chem. Front.*, 2018, **2**, 22–35.
10 M. Ghorbani-Asl, P. D. Bristowe and K. Koziołstrok, *Phys. Chem. Chem. Phys.*, 2015, **17**, 18273–18277.
11 K. Z. Milowska, M. Ghorbani-Asl, M. Burda, L. Wolanicka, N. Ćatić, P. D. Bristowe, *et al.*, *Nanoscale*, 2017, **9**, 8458–8469.
12 B. Guo, Y. Chen, Z. Wang, J. Yi, S. Ni, Y. Du, *et al.*, *Carbon*, 2020, **159**, 201–212.
13 F. Daneshvar, T. Zhang, A. Aziz, H.-J. Sue and M. E. Welland, *Carbon*, 2020, **157**, 583–593.
14 C. Shi, C. Deng, X. Zhang and P. Yang, *ACS Appl. Mater. Interfaces*, 2013, **5**, 7770–7776.
15 H. Lee, S. M. Dellatore, W. M. Miller and P. B. Messersmith, *Science*, 2007, **318**, 426–430.
16 Y. Liu, K. Ai and L. Lu, *Chem. Rev.*, 2014, **114**, 5057–5115.
17 W. Zhang, F. Yang, Y. Han, R. Gaikwad, Z. Leonenko and B. Zhao, *Biomacromolecules*, 2013, **14**, 394–405.

18 Z. Xu, *Sci. Rep.*, 2013, **3**, 2914.
19 H. Li, T. Marshall, Y. V. Aulin, A. C. Thenuwara, Y. Zhao, E. Borguet, *et al.*, *J. Mater. Sci.*, 2019, **54**, 6393–6400.
20 I. D. Rosca, F. Watari, M. Uo and T. Akasaka, *Carbon*, 2005, **43**, 3124–3131.
21 M. S. Hong, Y. Park, T. Kim, K. Kim and J. G. Kim, *J. Materiomics*, 2020, **6**, 158–166.
22 M. K. Rabchinskii, A. T. Dideikin, D. A. Kirilenko, M. V. Baidakova, V. V. Shnitov, F. Roth, *et al.*, *Sci. Rep.*, 2018, **8**, 14154.
23 T. Wirtz, O. De Castro, J. N. Audinot and P. Philipp, *Annu. Rev. Anal. Chem.*, 2019, **12**, 523–543.
24 R. Saeed, J. Schlegel, G. Castano, R. Carlos and R. Sawafta, *Int. J. Eng. Res. Sci. Technol.*, 2016, **5**, 405–412.
25 M. C. Biesinger, *Surf. Interface Anal.*, 2017, **49**, 1325–1334.
26 V. Ball, I. Nguyen, M. Haupt, C. Oehr, C. Arnoult, V. Toniazzo, *et al.*, *J. Colloid Interface Sci.*, 2011, **364**, 359–365.
27 D. A. Bulushev, A. L. Chuvilin, V. I. Sobolev, S. G. Stolyarova, Y. V. Shubin, I. P. Asanov, *et al.*, *J. Mater. Chem. A*, 2017, **5**, 10574–10583.
28 T. Susi, T. Pichler and P. Ayala, *Beilstein J. Nanotechnol.*, 2015, **6**, 177–192.
29 W. Tamakloe, D. A. Agyeman, M. Park, J. Yanga and Y. Kang, *J. Mater. Chem. A*, 2019, **7**, 7396–7405.
30 Y. Liao, Y. Wang, X. Feng, W. Wanga, F. Xua and L. Zhanga, *Mater. Chem. Phys.*, 2010, **121**, 534–540.
31 R. S. Vishwanath and K. Sakthivel, *J. Mater. Chem. A*, 2017, **5**, 2052–2065.
32 Y. Sohn, D. Pradhan, L. Zhao and K. T. Leung, *Electrochem. Solid-State Lett.*, 2012, **15**, K35.
33 A. Radi, D. Pradhan, Y. Sohn and K. T. Leung, *ACS Nano*, 2010, **4**, 1553–1560.
34 D. G. Barrett, D. E. Fullenkamp, L. He, N. Holten-Andersen, K. Y. Lee and P. B. Messersmith, *Adv. Funct. Mater.*, 2013, **23**, 1111–1119.
35 F. Wei, J. Liu, Y. Zhu, X. Wang, C. Cao and W. Song, *Sci. China: Chem.*, 2017, **60**, 1236–1242.
36 R. A. Zangmeister, T. A. Morris and M. J. Tarlov, *Langmuir*, 2013, **29**, 8619–8628.
37 G. Deroubaix and P. Marcus, *Surf. Interface Anal.*, 1992, **18**, 39–46.
38 J. Ghijsen, L. H. Tjeng, J. van Elp, H. Eskes, J. Westerink and G. A. Sawatzky, *Phys. Rev. B: Condens. Matter Mater. Phys.*, 1988, **38**, 11322.
39 H. Li, J. Xi, Y. Zhao and F. Ren, *MRS Adv.*, 2019, **4**, 405–412.
40 D. Mott, J. Galkowski, L. Wang, J. Luo and C. J. Zhong, *Langmuir*, 2007, **23**, 5740–5745.
41 A. Lekawa-Raus, K. Walczak, G. Kozlowski, S. C. Hopkins, M. Wozniak, B. A. Glowacki, *et al.*, *Scr. Mater.*, 2015, **106**, 34–37.
42 K. Ai, Y. Liu, C. Ruan, L. Lu and G. M. Lu, *Adv. Mater.*, 2013, **25**, 998–1003.
43 J. Kong, W. A. Yee, L. Yang, Y. Wei, S. L. Phua, H. G. Ong, *et al.*, *Chem. Commun.*, 2012, **48**, 10316–10318.
44 X. Yu, H. Fan, Y. Liu, Z. Shi and Z. Jin, *Langmuir*, 2014, **30**, 5497–5505.
45 A. Naeemi and J. D. Meindl, *IEEE Electron Device Lett.*, 2006, **27**, 338–340.
46 A. Naeemi and J. D. Meindl, *IEEE Electron Device Lett.*, 2007, **28**, 135–138.
47 M. M. Jastrzebska, J. Isotalo, J. Paloheimo and H. J. Stubb, *J. Biomater. Sci., Polym. Ed.*, 1996, **7**, 577.
48 A. B. Mostert, B. J. Powell, F. L. Pratt, G. R. Hanson, T. Sarna, I. R. Gentle, *et al.*, *Proc. Natl. Acad. Sci. U. S. A.*, 2012, **109**, 8943–8947.